

Ordering in stretch-tunable polymeric opal fibers

Chris E. Finlayson,¹ Chris Goddard,² Elpida Papachristodoulou,¹ David R.E. Snoswell,¹ Andreas Kontogeorgos,¹ Peter Spahn,³ G.P. Hellmann,³ Ortwin Hess,^{2*} and Jeremy J. Baumberg^{1*}

¹NanoPhotonics Centre, University of Cambridge, Cambridge CB3 0HE, UK

²Blackett Laboratory, Imperial College London, South Kensington Campus, London SW7 2AZ, UK

³Deutsches Kunststoff-Institut (DKI), Schlossgartenstrasse 6, D-64289 Darmstadt, Germany

*jjb12@cam.ac.uk, o.hess@imperial.ac.uk

Abstract: We demonstrate the production of high-quality polymer opal fibers in an industrially-scalable process. These fibers exhibit structural color, based on the self-assembly of sub-micron core-shell particles, with a spectrum which is stretch-tunable across the visible region. The internal substructure and ordering of fibers, as inferred from variations in spectral bandwidth, is studied using dark-field microscopy. We employ a granular model to examine flow and shear forces during the extrusion process, and the effects on particle ordering. In both theory and experiment, a concentric zone of the fiber near the exposed surface develops particularly strong structural color. Such elastically-tuned structurally colored fibers are of interest for many applications.

©2011 Optical Society of America

OCIS codes: (160.5470) Polymers; (160.4670) Optical materials; (230.5298) Photonic crystals.

References and links

1. T. Ruhl, P. Spahn, and G. P. Hellmann, "Artificial opals prepared by melt compression," *Polymer* (Guildf.) **44**(25), 7625–7634 (2003).
2. O. L. J. Pursiainen, J. J. Baumberg, K. Ryan, J. Bauer, H. Winkler, B. Viel, and T. Ruhl, "Compact strain-sensitive flexible photonic crystals for sensors," *Appl. Phys. Lett.* **87**(10), 101902 (2005).
3. B. Viel, T. Ruhl, and G. P. Hellmann, "Reversible deformation of opal elastomers," *Chem. Mater.* **19**(23), 5673–5679 (2007).
4. O. L. J. Pursiainen, J. J. Baumberg, H. Winkler, B. Viel, P. Spahn, and T. Ruhl, "Nanoparticle-tuned structural color from polymer opals," *Opt. Express* **15**(15), 9553–9561 (2007), <http://www.opticsinfobase.org/oe/abstract.cfm?URI=oe-15-15-9553>.
5. O. L. J. Pursiainen, J. J. Baumberg, H. Winkler, B. Viel, P. Spahn, and T. Ruhl, "Shear-induced organization in flexible polymer opals," *Adv. Mater.* **20**(8), 1484–1487 (2008).
6. D. R. E. Snoswell, A. Kontogeorgos, J. J. Baumberg, T. D. Lord, M. R. Mackley, P. Spahn, and G. P. Hellmann, "Shear ordering in polymer photonic crystals," *Phys. Rev. E Stat. Nonlin. Soft Matter Phys.* **81**(2 Pt 1), 020401 (2010).
7. B. J. Ackerson, and P. N. Pusey, "Shear-induced order in suspensions of hard spheres," *Phys. Rev. Lett.* **61**(8), 1033–1036 (1988).
8. Y. A. Vlasov, X.-Z. Bo, J. C. Sturm, and D. J. Norris, "On-chip natural assembly of silicon photonic bandgap crystals," *Nature* **414**(6861), 289–293 (2001).
9. M. D. Haw, W. C. K. Poon, and P. N. Pusey, "Direct observation of oscillatory-shear-induced order in colloidal suspensions," *Phys. Rev. E Stat. Phys. Plasmas Fluids Relat. Interdiscip. Topics* **57**(6), 6859–6864 (1998).
10. R. De La Rue, "Photonic crystals: Microassembly in 3D," *Nat. Mater.* **2**(2), 74–76 (2003).
11. J. J. Baumberg, O. L. Pursiainen, and P. Spahn, "Resonant optical scattering in nanoparticle-doped polymer photonic crystals," *Phys. Rev. B* **80**(20), 201103 (2009).
12. P. Vukusic, and J. R. Sambles, "Photonic structures in biology," *Nature* **424**(6950), 852–855 (2003).
13. Strain, e , where $e = 100\% \times \Delta l/l$, or % increase in length.
14. A. Kontogeorgos, D. R. Snoswell, C. E. Finlayson, J. J. Baumberg, P. Spahn, and G. P. Hellmann, "Inducing symmetry breaking in nanostructures: anisotropic stretch-tuning photonic crystals," *Phys. Rev. Lett.* **105**(23), 233909 (2010).
15. M. Kolle, B. Zheng, N. Gibbons, J. J. Baumberg, and U. Steiner, "Stretch-tuneable dielectric mirrors and optical microcavities," *Opt. Express* **18**(5), 4356–4364 (2010).

16. C. E. Finlayson, P. Spahn, D. R. E. Snoswell, G. Yates, A. Kontogeorgos, A. I. Haines, G. P. Hellmann, and J. J. Baumberg, "3D bulk-ordering in macroscopic solid opaline films by edge-induced rotational-shearing," *Adv. Mater.* doi 10.1002/adma.201003934 (to be published).
17. J. Batchelor, J. P. Berry, and F. Horsfall, "Die swell in elastic and viscous fluids," *Polymer (Guildf.)* **14**(7), 297–299 (1973).
18. P. C. Hiemenz, and T. P. Lodge, in *Polymer Chemistry*, 2nd ed. (CRC Press, London, 2007)
19. T. Ruhl, and G. P. Hellmann, "Colloidal crystals in latex films: Rubbery opals," *Macromol. Chem. Phys.* **202**(18), 3502–3505 (2001).
20. L. Verlet, "Computer 'Experiments' on Classical Fluids. I. Thermodynamical Properties of Lennard-Jones Molecules," *Phys. Rev.* **159**(1), 98–103 (1967).
21. L. Verlet, "Computer 'Experiments' on Classical Fluids. II. Equilibrium Correlation Functions," *Phys. Rev.* **165**(1), 201–214 (1968).
22. H. J. C. Berendsen, J. P. M. Postma, W. F. van Gunsteren, A. DiNola, and J. R. Haak, "Molecular dynamics with coupling to an external bath," *J. Chem. Phys.* **81**(8), 3684–3690 (1984).
23. M. Oda, and K. Iwashita, in *Mechanics of granular materials: an introduction* (Taylor & Francis, London, 1999)
24. T. Ruhl, P. Spahn, H. Winkler, and G. P. Hellmann, "Large Area Monodomain Order in Colloidal Crystals," *Macromol. Chem. Phys.* **205**(10), 1385–1393 (2004).

1. Introduction

A low-cost, industrial-scale technique to produce flexible opals has recently been developed using melting and shear-ordering of core/shell polymer nanoparticles [1–6]. This produces low-defect flexible polymer *fcc* opals films with fundamental optical resonances tunable across the visible and near-infrared regions (by varying the precursor nano-sphere size from 200 to 350nm, and hence the resulting *fcc* lattice parameter). Such polymeric opals have intrinsic advantages over other self-assembling colloidal systems [7–10], in that the structures formed are solvent-free and permanently formed as a solid. In the lower refractive-index contrast regime associated with these polymer composites, color generation arises through spectrally-resonant scattering inside a 3D *fcc*-lattice photonic crystal [11], as opposed to normal reflective iridescence based on Bragg diffraction. This principle is of fundamental interest in understanding the origins of structural colors and iridescence in natural opals, such as those in minerals or in biological structures [12]. In addition, one of the most attractive features of elastomeric polymer opals is the tunability of their perceived color by the bending or stretch modification of the (111) plane spacing. Such properties raise the possibility of producing finely drawn or extruded opaline fibers, utilizing strong structural color effects as a replacement for toxic and photodegradable dyes in a variety of materials, such as clothing fabrics. However, since ordering proceeds from outer flat surfaces which seed accumulation of (111) planes, it is far from obvious that opal fibers can be produced [6].

In this paper, we report the fabrication (by extrusion) and characterization of high-quality polymer opal fibers in an industrially-scalable process. The fibers have sufficient mechanical robustness to demonstrate the anticipated stretch-tunable structural color. The fibers show a significant amount of internal substructure, as observed using dark-field microscopy. The correlation of this concentric substructure with zones of different degrees of particle ordering is further investigated, both spectroscopically and using a granular model to gain a further understanding of flow and shear forces during the extrusion process. Whilst the as-extruded fibers have a readily visible structural color, we typically find that a concentric zone just below the exposed surface is characterized by particularly strong structural color. Suitable methods by which this color may be accessed are discussed.

1.1 Polymer opal fiber fabrication

The fabrication technique employed uses shear-flow self-assembly of polymer particles into a 3D face centered cubic (*fcc*) lattice, through extrusion at high temperatures. As illustrated in Fig. 1(a), the core-shell particle precursors are approximately 300nm in diameter, and consist of a hard polystyrene (PS) core, coated with a thin polymer layer containing allyl methacrylate (ALMA) as a grafting agent, and a soft polyethylacrylate (PEA) outer-shell [1,3]. The mini-extruder (Thermo Scientific, *MiniLab*) consists of two counter rotating metallic screws with

adjustable speed in the range 1-150 rotations per minute (rpm) and adjustable temperature 25-250°C. Up to 6g of the opal precursor materials are manually driven into the extruder, where they form a melt and are homogenized under the extreme shear forces provided by the screws. The overpressure generated then drives the shear-ordered granular material through a narrow-bore stainless steel die, producing thin opaline fibers (see Figs. 1b and c).

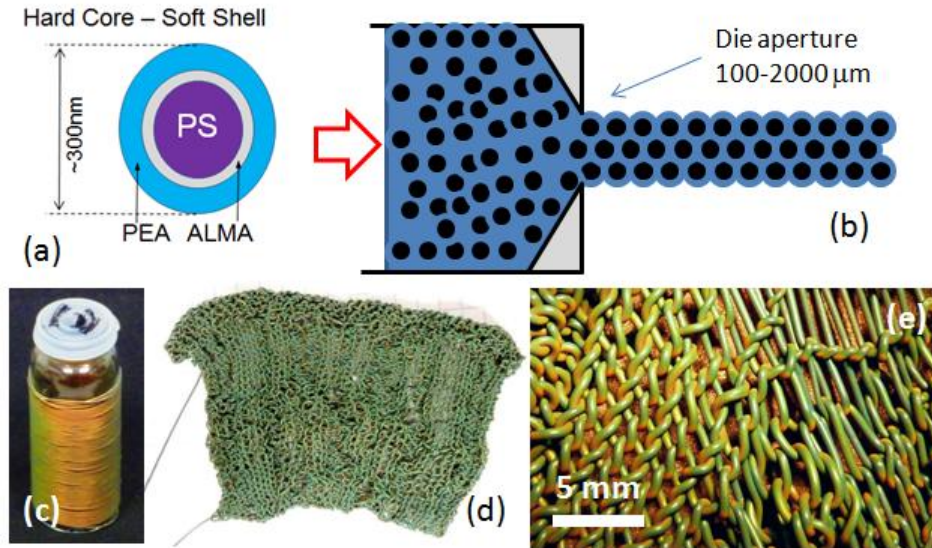


Fig. 1. (a) Schematic of core-interlayer-shell system, based on polystyrene (PS)-allyl methacrylate (ALMA)-polyethylacrylate (PEA), used for polymer opal production. (b) Fiber extrusion process, illustrating how the viscous ensemble of CIS particles is forced through a die aperture (not to scale) under pressure to produce long fibers of opaline quality, as shown in (c). Cross-linked fibers may be knitted into fabrics (d), with a marked stretch-variable structural color effect (e).

The extruded fibers described in this paper were made from a red opal (core diameter $\sim 250\text{nm}$) with OH- functionality, mixed together with 0.1% wt of sub-50nm carbon black particles and 2% wt of benzophenone. The introduction of a small fraction of carbon nanoparticle dopants into the interstices of the photonic crystal lattice does not disrupt the lattice quality but results in a remarkable change in the color of the opals, from a milky white to intense orange/red via spectrally-resonant scattering [4]. The color saturation is also seen to increase with the concentration of carbon. The benzophenone is needed for later post-crosslinking of the fibers.

The material was recycled in the extruder three times in order to fully homogenize the opal/carbon mixture. Finally, the fibers were extruded at 120°C with screw speed $\sim 30\text{rpm}$. Fibers with diameters between $100\mu\text{m}$ and $2000\mu\text{m}$ were extruded at constant screw speed, in order to study the relation of the fiber diameter to the internal substructure. Crosslinking was achieved by then curing in UV-A light for 30 minutes. The final fiber products have sufficient mechanical robustness to allow them to be hand-knitted into stretchable fabrics, as illustrated in Figs. 1(d) and (e).

2. Experimental characterization

2.1 Stretch tuning of structural color

The polymer opal fibers show significant changes in color as they are stretched. Figure 2 shows both visually and spectroscopically how the color changes in a $1000\mu\text{m}$ diameter sample from red through yellow/green, blue, and finally to a grayish color, as the strain [13] increases from $e = 0$ to 50%. These color changes are due to the decrease of the inter-planar

distance during stretching, as explained by Bragg diffraction. During the stretching of fibers, spheres within each plane parallel to the surface move apart but planes normal to the surface move closer to each other in order to keep the total volume constant, which causes the Bragg wavelength to shift to lower values [14]. There is hence a roughly linear variation of strain with peak wavelength, as expected from straining polymer multilayers [15]. The dark field reflectance for different strains is shown in Fig. 2(b). This reveals a sharp resonance (FWHM ~ 40 nm) in scattered light for the unstretched fiber, corresponding to the marked red appearance which is seen visually at near-normal incidence. As the fiber becomes increasingly stretched, the spectra are blue-shifted, but also become notably broader in bandwidth, as the ensemble of core-shell particles is transformed from *fcc* to a monoclinic lattice with strain [14]. For e greater than $\sim 50\%$, the spectra become very flat and broad, as expected from the pale gray appearance of the fiber.

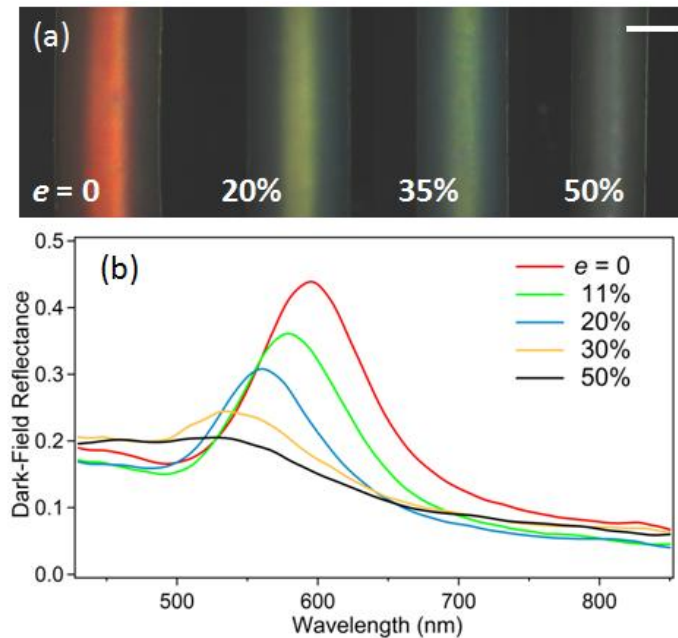


Fig. 2. (a) Dark-field $\times 5$ images of $1000\ \mu\text{m}$ diameter red-opal fiber at strains (left to right, in montage) of $e = 0$, 20%, 35% and 50%. The scale bar is $500\ \mu\text{m}$ long. (b) Corresponding dark-field reflectance spectra for different strains.

The effect of stretching on ordering and coloring of fibers is however *reversible*, given that the cross-linked fibers have not exceeded the elastic limit for $e < 50\%$. Similar color changes from red to blue/grey are also observed when fibers of other diameters are stretched. Typically, the degree of spectral-shift is measured to be between -2.5 and -3.0 nm per % of strain. The rate of color tuning with strain is seen to be rather smaller in the narrow diameter fibers, probably on account of the higher surface-to-volume ratio allowing a more effective cross-linking and less visco-elastic effect in that case. Hence, such fibers can be utilized in applications as diverse as textiles or photonic devices, for instance as matching filters surrounding cylindrical organic solar cells.

2.2 Substructure in extruded fibers

The fibers were carefully cross-sectioned using specially devised techniques (detailed in Appendix A). From the images of the transverse cross section of fibers (Fig. 3), it is apparent that the interior of the fiber is not homogeneous. The substructure of the fibers generally consists of a series of concentric circular zones of different color. From the example of the

2000 μm diameter fiber in Fig. 3a, we identify three main zones; a thin, dull-green outer ring of thickness 30-40 μm , followed by a larger red zone which becomes more orange-yellow towards the centre, and finally an inner green central part. The exact boundaries of the three regions are not obvious visually, since the color changes are gradual and sensitive to image color balance. Hence spectroscopic mapping of the cross-sections is preferred for detailed comparisons.

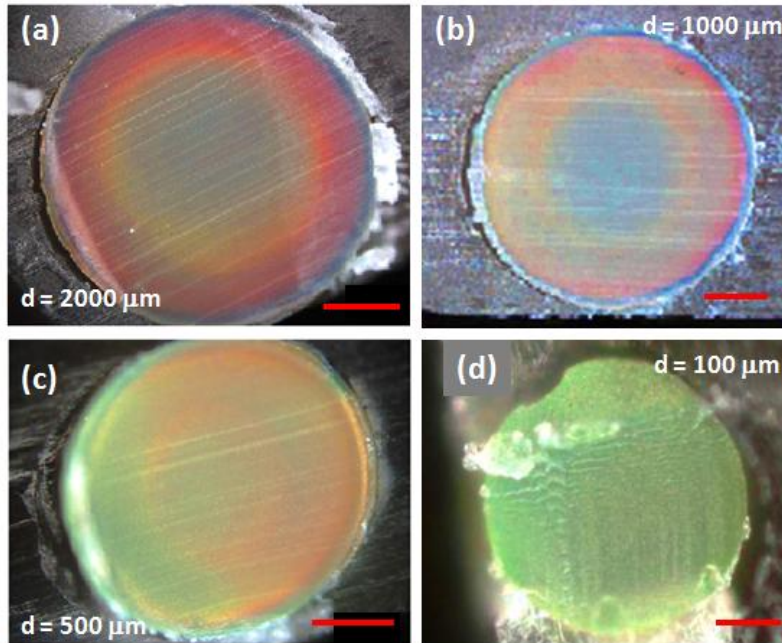


Fig. 3. Dark-field microscopy images of transverse cross-sections of red-opal fibers, showing concentric substructure. The fiber diameters, d , are as indicated; the scale bars have lengths of (a) 500 μm , (b) 250 μm , (c) 200 μm and (d) 25 μm .

Similar substructure is also observed for the 1000 μm diameter fiber (Fig. 3b), but with a significant decrease in the width of the ordered red zone. For thinner fibers, the substructure appears somewhat different, with the concentric red zones becoming less well defined for the 500 μm fiber and absent for the 100 μm fiber. Of significance is the difference in extrusion speeds for these fibers; to a first approximation, this speed is inversely dependent on the cross-sectional area of the die nozzle (Fig. 1b). The 2000 μm fiber was extruded at a few mm/sec, whereas the very fine diameter fibers have relatively high nozzle speeds exceeding 10s of cm/sec, which may suppress opaline ordering [16]. Additionally, the effects of “die swell” [17,18] as the fibers leave the extruder under pressure are expected to be proportionally more significant for the smaller diameters. This is due to faster extrusion and hence greater compression in the die channel; when the fiber emerges, there is a significant “rebound” effect and shear-mixing. To illustrate this, in Table 1, the fiber diameters are compared with the die diameters. Some swelling is evident in each case, with the 100 μm fiber showing the greatest proportional deviation. Commensurately, the lattice constant is notably increased in the thinnest fiber compared to the wider fibers, as inferred from the blue-shift in peak spectral wavelength at the zone of best ordering (Table 1).

As a quantitative measure of the ordering in the different concentric zones of the fibers, dark-field scattering spectra are shown in Fig. 4(a), with spectra being collected at different points across the transverse cross-section of a 2000 μm diameter fiber. The wavelength of the scattering peak against radial distance from the center (Fig. 4b) confirms the presence of these zones (shaded). Moving radially away from the centre the peak shifts across the red zones and

outwards to the greenish outer layer. The peak heights in cross-sections typically observed are not as intense as those shown in Fig. 2, where measurements are taken at normal incidence to the (111) planes of the opaline crystal parallel to the surface, where scattering will be strongest.

Lorentzian functions are fitted to the spectra above (where the lineshape results from disorder averaging, see [6]), in order to estimate the full-width half maximum (FWHM) associated with different concentric zones. Hence the depth of greatest ordering is ascertained to be 120 μm below the fiber surface (Fig. 4b) for the 2000 μm diameter fibre. Furthermore, the outermost green zone of depth 30-40 μm is more poorly ordered (with the largest linewidth) than any inner zone of the fiber. This additional poorly ordered outer layer is not found for processed flat *film* geometries, and possibly arises from the strong surface forces arising from the die swell on exit of the cylindrical fiber.

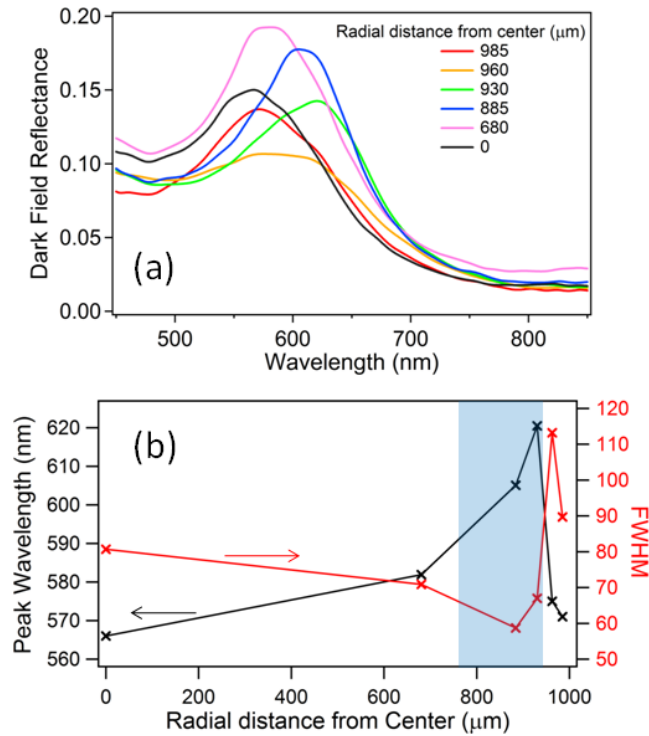


Fig. 4. (a) Dark-field reflectance spectra collected at increasing radial positions on the fiber transverse cross-section shown in Fig. 3(a) (radius = 1000 μm). (b) Peak wavelength and spectral FWHM of spectra as a function of radial distance from the fiber centre. The blue-shaded region indicates the zone of best ordering, where the FWHM < 70 nm

Table 1. Comparison of the measured diameter of extruded fibers with the die diameter, together with the peak spectral wavelength (dark-field) at the zone of best ordering.

Extruder die diameter (μm)	Measured fiber diameter (μm) $\pm 10 \mu\text{m}$	Estimated "die swell" in diameter (%)	Peak wavelength (nm) at zone of lowest FWHM
2000	2020	1.0	605
1000	1025	2.5	597
500	525	5.0	598
100	110	10	571

2.3 Post-extrusion processing

In recent work the ordering in thin-films of polymeric opals was observed to undergo a remarkable improvement by using an edge-shearing technique to give enhanced structural color effects [16]. In this method extruded ribbon samples encapsulated between polyester tapes are pressed into films and passed once over a right-angle edge heated at 150°C. However, attempts to employ this method with extruded fibers were not successful, as the fiber becomes molten and disintegrates under tension almost immediately.

A different approach is to remove the outermost layer of the fiber post extrusion, in order to leave the zone of best opaline ordering from underneath exposed. Whilst this may be possible using a polishing or “splicing” process, for the purposes of this study, we take angled *longitudinal* cross-sections of the fiber in order to access the internal substructure. The geometry of such angled cross-sections, in comparison to the transverse methods described earlier, is illustrated in Fig. 5. As seen both from the image and spectra, sectioning down to a depth of ~30 μm below the fiber surface successfully reveals an enhancement of the dark-field intensity and decreased spectral FWHM together with the expected shift to longer wavelengths seen in the transverse spectra. Hence the optimal opaline ordering is confirmed to be buried under the surface as compared to typical shear-ordering opals.

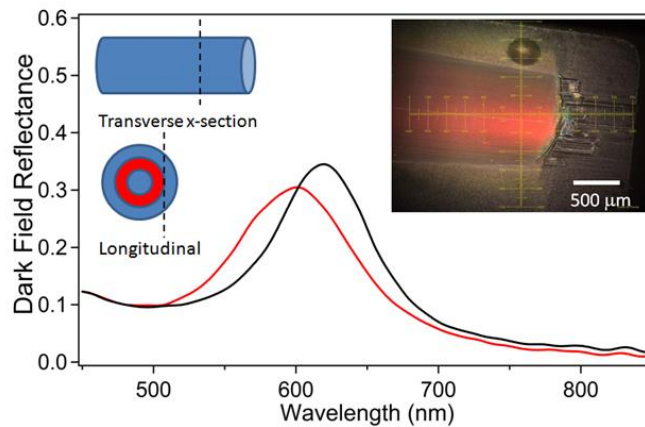


Fig. 5. Dark-field reflectance spectra of a 2000 μm diameter fiber before (red) and after (black) longitudinal cross-sectioning. The left inset shows the relative geometries of transverse and longitudinal cross-sectioning of fibers. The right inset shows an image of the exposed surface of the red opal after longitudinal sectioning, with the point at which spectrum was collected being at the centre of the overlaid cross-hairs.

3. Granular models of fiber extrusion

With the following simulations we aim to gain understanding of the mechanism by which sphere order develops through flow. A simple generic model for spheres is introduced, and through non-equilibrium interparticle dynamics (NEID) the interactions in a wire geometry are studied.

The flow of polymer opals can be modeled as a granular system of particles as there is no solvent to be considered (solvent can be considered as carried locally in the soft shell around each sphere core [19]). Each 'particle' is represented as a soft sphere interacting through a radial pairwise potential with other spheres. The force (in rescaled units) between two spheres is characterized by a strong repulsion from the hard sphere core, combined with an attraction for spheres which are in contact to reproduce the 'sticky' nature of the interaction. Using the ratio of core-interlayer-shell radii provided in [19] as a guide, a simple model (Eq. (1)) is created for this force as shown in Fig. 6.

$$F(r) = -r^{-14} - 14r + 16, \quad r < r_0. \quad (1)$$

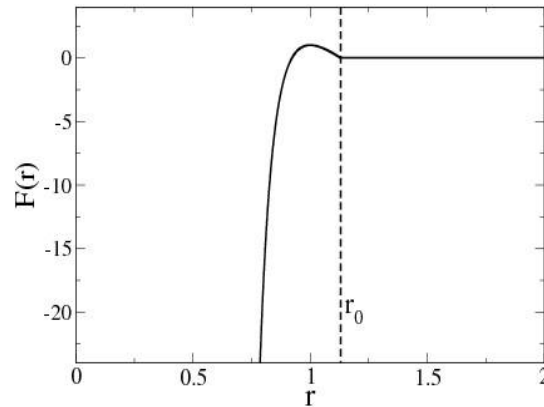


Fig. 6. Force between two spheres, as given by Eq. (1). $F(r)$ is set as zero for values of $r > r_0$.

The maximum attractive force is given at a separation distance of $r = 1$ in rescaled units. Since there is no relevant force between spheres which are not touching, a cut off at r_0 (sphere radius) is used to complete the model. The total force on a sphere is calculated from the sum of the forces from all interacting spheres. Time integration is handled by a velocity Verlet algorithm [20,21] and a Berendsen velocity scaling thermostat [22] is used to damp the energy of system and control the temperature. Simulation units are rescaled to the sphere diameter and mass, while time rescaling is introduced from the force normalisation.

A cylindrical geometry is chosen to model flow through a circular channel pre-extrusion. The ordering process is studied in this isolated region with periodic boundary conditions along the flow axis. An external flow field corresponding to that of a Poiseuille flow is imposed on the system to generate a flow in the required direction. Smooth wall boundary conditions are considered for the simulations, whereby spheres interacting with the wall are subject to a repulsive normal force depending on their distance.

The following simulations are used to represent a section of very small diameter fiber, and for a short period of time due to the computational limitations of the NEID method. We focus on the origin and initial spread of order from a completely disordered state. A measure for the local order of the system is calculated for each sphere. Pairs of nearest 'in plane' neighbours are identified and the angles between them measured for their deviation from an *fcc* arrangement. The average value of this deviation is then used to color spheres in the visualizations so that dark regions are well ordered. The local stress acting on each sphere is also calculated from interactions over the surface of the sphere [23].

In the simulation shown in Fig. 7, ordered regions are observed developing at the surface boundary of the fiber. These initially grow locally along the face of the boundary, but eventually spread inwards once the order has developed to a large enough area to seed further templating inwards. After sufficient time ($t = 50$ here) the order is developed, and a balance between ordered skin and disordered core is obtained.

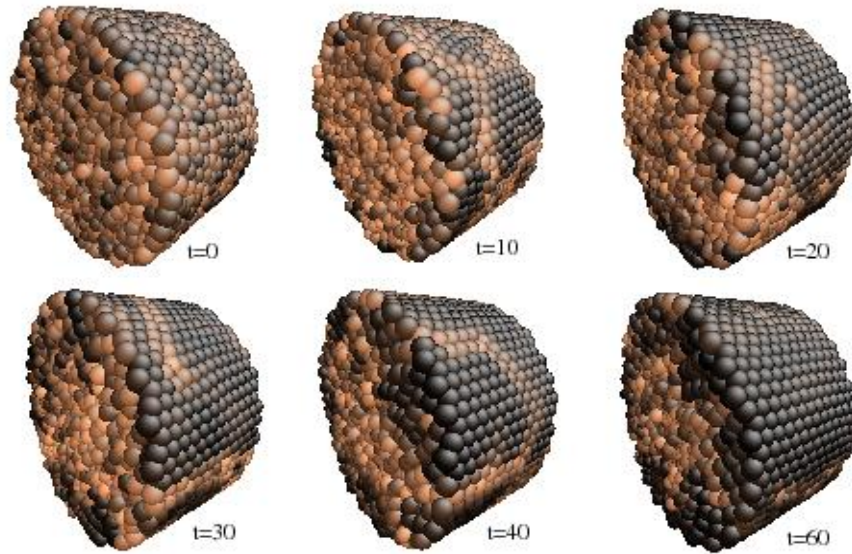


Fig. 7. Snapshots in time for a simulation of 5000 spheres. The darker color corresponds to higher local order.

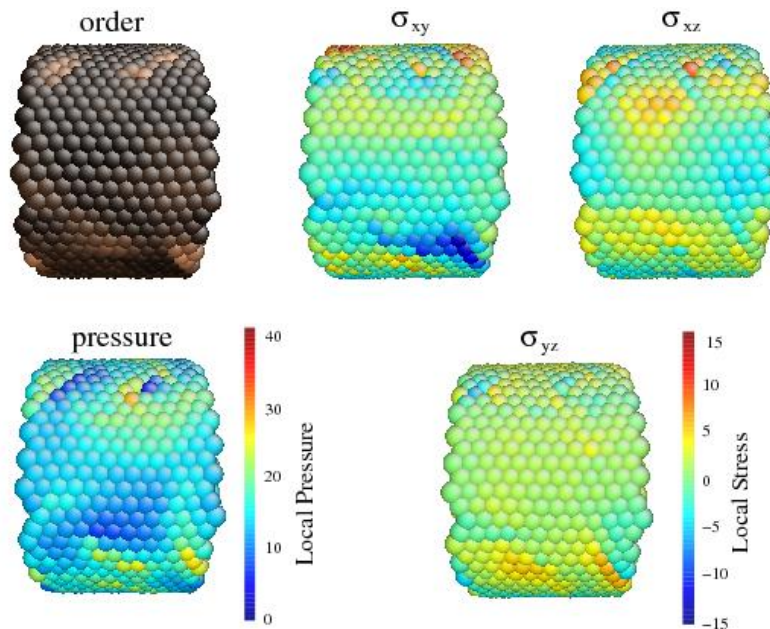


Fig. 8. Snapshot of a region of the wire showing the surface order along with corresponding stress and pressure measurements. Defects show correlation with regions of higher pressure and stress.

The components of shear stress (σ) in the ordered regions of each layer are low compared to values in the unordered regions, as shown in Fig. 8. The unordered regions also show discontinuities in stress and pressure. In these regions of disorder the spheres have been transported by the flow field into arrangements where contacts are too close, and the forces between spheres (and hence the resulting stresses) are high. Conversely, ordered regions appear to move together in a ‘jammed’ state, distributing the forces efficiently and smoothly.

Layers of spheres are then able to slide past each other to create flow. When simulations are continued, the fiber segment continues to get more ordered. The areas of disorder and corresponding defects disappear as the flow progresses and order spreads.

3.1 Qualitative comparisons with experimental results

The granular modeling of fiber extrusion described in this section successfully predicts many of the experimentally observed phenomena. In particular, the higher pressure and stresses associated with areas of disorder leads to the disappearance of corresponding defects as the flow progresses. Hence, well-ordered regions are predicted to evolve radially inwards from the walls within the extrusion channel. This correlates strongly with the substructures shown in Fig. 3, where there is clear evidence of concentric zones and better ordering in the outer zones.

In the regimes of flow rates and die apertures being studied, and assuming viscosity coefficients of $\sim 10^4$ Pa.sec, as reported in our previous work [6], it can readily be shown that Reynolds number for the extrusion process is $Re \ll 1$ and that a simple Poiseuille flow model is therefore justified. However, the model uses flow rate and time parameters, which may not be sufficient to predict the same evolution of ordering in fast-extruded, thin fibers. Experimentally, much slower and perhaps less practicable extrusion rates may result in a commensurate better ordering in these narrow diameter fibers.

The models do not yet predict the less well-ordered buried surface layer, which is typically characteristic of extruded fibers. More sophisticated theoretical approaches, including finite friction conditions at the walls may be required in this respect. In addition it may be necessary to model the real effect of the fiber exiting the die, and the corresponding die swell region. However the model successfully predicts formation of ordered close-packed layers on the outer region of the fiber, and the growth of this order inwards from these seed layers.

4. Conclusions and outlook

The fabrication (by extrusion) and characterization of high-quality polymer opal fibers, in an industrially-scalable process, is reported. These fibers exhibit structural color, based on the self-assembly of sub-micron core-shell particles, within a solvent-free granular system. The fibers have sufficient mechanical robustness to demonstrate the anticipated stretch-tunability. The internal substructure and ordering of fibers is studied using dark-field microscopy. The correlation of concentric substructure with zones of different degrees of particle ordering is further investigated, both spectroscopically and using a granular model to gain a further understanding of flow and shear forces during the extrusion process. Whilst the as-extruded fibers have a readily visible structural color, we find a concentric zone, just below the exposed surface, possesses extremely strong color. This structurally-colored skin may be accessed by post-extrusion processing.

Elastomeric polymer opal fibers have many attractive functional features; intense structural color, with inherent stretch- and bend-tunability, and excellent durability and mechanical robustness. These fibers are thus potential candidates for a novel range of nano-materials and clothing fabrics, utilizing strong structural color effects as a replacement for toxic and photodegradable dyes.

Appendix A; experimental methods

A.1 Polymer synthesis

The core-shell particle precursors were synthesized by semi-continuous, stepwise emulsion polymerization as described earlier [24]. Starved-feed conditions were maintained throughout the synthesis and surfactants were used in the lowest amount possible to ensure the development of accurate particle architecture and to avoid secondary nucleation. Polystyrene, crosslinked with 10% wt of butanediol diacrylate, was polymerized first. The polystyrene

particles were subsequently coated with a copolymer of ethyl acrylate and 10% wt of allyl methacrylate as an interlayer for grafting of the shell polymer. Finally a shell of polyethylacrylate was synthesized. To reduce the stickiness and enhance the toughness of the polymer, the glass transition temperature of the shell polymer was increased to -1°C by copolymerization of the ethyl acrylate with 3% wt hydroxyethyl methacrylate, 25% wt isobutyl methacrylate and 0.2% wt of diallyl phthalate. The ratio of core: interlayer: shell was 33: 10: 57 by wt.

A.2 Microscopy

Fibers were cross-sectioned for microscopy by carefully placing samples in molten dental wax and then setting to hardness by cooling with liquid nitrogen. Thin microtomes of the sample were then removed with a micro-positioned glass knife-edge, at room temperature, until a suitably clean cross-section of the film was visible at the surface of the wax. All the microscopic images displayed were then taken with an Olympus BX51 light microscope.

A.3 Spectroscopy

All spectroscopic measurements reported were taken with an adapted Olympus BX51 microscope, using a focused spot diameter of approximately $2\ \mu\text{m}$ (at $\times 20$ magnification), with the light signal collected using suitable focusing optics and a fiber-coupled CCD spectrometer. The spectra were standardized using a diffusive white-light scatterer (for dark-field reflectance).

A.4 Stretching experiments

The effect of stretching on the color of the fibers was studied by taking spectra from the surface of the fibers at different measured strains (e , where $e = 100\% \times \Delta l/l$, or % increase in length). Pieces of length $\sim 10\text{cm}$, equal to the circumference of a glass vial, were coiled around the vial and securely taped down. The circumference of the vial was systematically marked with 10% strain factor steps. The fibers were stretched until the ordering of particles was completely lost or the fiber broke. The vial was positioned carefully under the BX51 microscope, with the radial direction of the fiber always being normal to the focal plane of the objective, and the same protocols for spectroscopy were used as described above.

Acknowledgments

This work was supported by EPSRC (UK) grants EP/G060649/1, EP/E040241. The authors thank Kathryn Phillips for knitting the fabrics illustrated in Figure 1 and R. Hardy of the Cavendish Laboratory for technical assistance.